THERMAL-CAPILLARY ANALYSIS OF SMALL-SCALE FLOATING ZONES: STEADY-STATE CALCULATIONS

Jacques L. DURANCEAU and Robert A. BROWN

Department of Chemical Engineering and Materials Processing Center, Massachusetts Institute of Technology, Cambridge, Massachusetts 02139, USA

Galerkin finite element analysis of a thermal-capillary model of the floating zone crystal growth process is used to predict the dependence of molten zone shape on operating conditions for the growth of small silicon boules. The model accounts for conduction-dominated heat transport in the melt, feed rod and growing crystal and for radiation between these phases, the ambient and a heater. Surface tension acting on the shape of the melt/gas meniscus counteracts gravity to set the shape of the molten zone. The maximum diameter of the growing crystal is set by the dewetting of the melt from the feed rod when the crystal radius is large. Calculations with small Bond number show the increased zone lengths possible for growth in a microgravity environment. The sensitivity of the method to the shape and intensity of the applied heating distribution is demonstrated. The calculations are compared with experimental observations.

1. Introduction

Since its invention by Pfann over 25 years ago [1,2], the floating zone or zone refining process has been a mainstay for the purification of solids and the production of single-crystal semiconductors. Small-scale floating zones are formed by translating a short circumferential heater along the axis of a cylindrical polycrystalline feed rod, as shown in fig. 1. A molten zone forms just ahead of the heater, is held in place by surface tension force acting against gravity, and is resolidified into a single-crystal rod along the stern of the heater. The size of the zone is governed by heat transfer between the melt and solid phases with the surrounding ambient and heater, and is limited by instabilities in the shape of the melt.

Beginning with the small-scale experiments of Pfann, the floating zone process has been refined so that single-crystal boules of silicon can be systematically grown that are 3–5 inches in diameter [3]. Most of the progress in this development has been based on empiricism. Although theoretical studies of the heat transfer [4–6], fluid mechanics (e.g. see refs. [7–11]), solute transport in the melt [12], and the role of surface tension in setting the shape and stability of the molten zone [13–17] have all been undertaken separately for idealized geometries, there is very little understanding of the integrated dynamics of the floating zone process. The goal of this research is to develop an integrated model that accounts for the roles of heat transfer and capillarity in small-scale floating zones and to use the model to predict the operating states and stability of the process.

The coupling of heat transport and capillarity in meniscus-defined crystal growth systems, where the melt is partially shaped by a melt-gas meniscus held in place by surface tension, requires complete models described in terms of highly nonlinear free-boundary problems for the locations of the melt/crystal and melt/feed interfaces and the meniscus shape, as well as the temperature field. The thermal-capillary model presented in section 2 includes these effects, but is based on only conduction in the melt and radiation
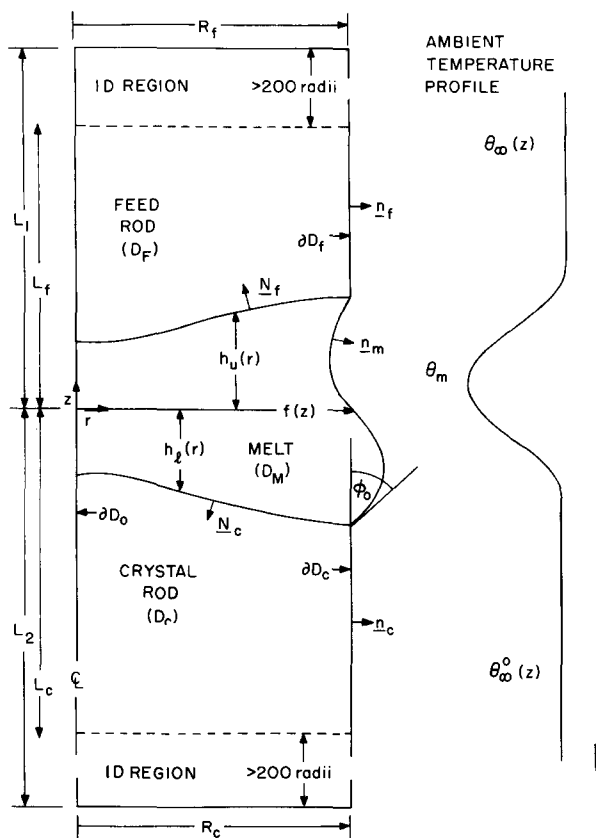
Fig. 1. Schematic of small-scale floating zone system modelled here.

between a distributed heat source and the floating zone. Numerical calculations of buoyancy-driven and surface-tension-driven flows in idealized geometries [9,18] suggest that large temperature differences are required for the bulk flow to intense enough to influence heat transport in the melt for small scale floating zones. The conduction-dominated model is expected to be quantitatively accurate when the Peclet numbers for heat transfer in the melt scaled with the speeds characteristic of these flows are small compared to unity. Accurate estimation of the magnitudes of these flows requires computation of the temperature field. The results of the thermal-capillary model are used for this purpose in section 6.

Even when heat transport is unaffected by bulk flow in the melt, dopant redistribution is set by the melt flow because of the magnitude of the ratio of the heat to mass diffusivities ($O(10^3)$) [12]. Then the details of the melt flow, especially oscillations induced by transitions in strong thermocapillary flows [17,19,20] are important in determining compositional striations in the crystal. Accurate prediction of the structure of these motions and of the conditions for transition from steady-state to oscillatory flow depend on the thermal boundary conditions and heat transport in the entire system. The calculations presented here are a first step toward the construction of such a model.

One of the most difficult aspects of modelling heat transport in the floating zone is representing heat exchange between the melt/crystal and feed materials with the ambient and the heater. Quantitative modeling requires a system-specific description of the heater which can only come from integrating experimental measurements with the calculations. We develop the thermal model for a heater which releases radiant energy distributed according to a general analytic temperature distribution. The thermal

ambient seen by the zone is modelled in a similar way. The usefulness of this approach in fitting experimental data is demonstrated in section 5.

We have developed a new numerical procedure, based on the Galerkin finite element method, for simultaneously computing the field variables and the interface shapes in meniscus-defined solidification processes [21,22]. The isotherm/Newton method used in those studies and extended here to a thermal capillary model of the floating zone is built on using Newton's method for solution of the full set of nonlinear residual equations resulting from the Galerkin finite-element discretization of the energy equations in each phase, the isotherm condition for the shapes of the melt/solid phase boundaries, and the Young–Laplace equation for the meniscus shape. Implementation of Newton's method for a free-boundary problem has the advantage of rapid convergence in all variables for steady-state calculations, as well as being the foundation of computer-implemented perturbation calculations for detecting solution multiplicity and determining stability [16,23]. The Newton iteration is also used in implementing time integration methods that are fully implicit in both the field and interface variables [24,25]. The formulation of the Newton iteration for the thermal-capillary model of the floating zone presented in section 3.

Understanding the effects of the coupling between heat transfer and capillarity on the overall stability and control of the floating zone process in one of the important applications of a detailed thermal-capillary analysis. The operating regions, expressed in terms of the heater shape and power and the sizes of the feed and crystal rods are limited because of the interaction of surface tension and heat transfer. Previous stability analyses of the floating zone process have either treated the melt as a liquid drop captured between two non-interacting cylindrical rods [13,16,26,27] or have accounted for the fact that the size of the growing crystal can respond to perturbations in the molten zone shape, but neglected the role of heat transport in setting this response [17]. For example, surface tension can only support the weight of a molten zone against the force of gravity within specific limits of zone length and radius given by static meniscus shapes and their stability predicted from the Young–Laplace equation; see refs. [13,16]. Lengthening the zone beyond these bounds causes the meniscus either to fail because of the loss of a stable static state or to recede across the top feed crystal when the angle formed between the meniscus and the melt/solid interface is decreased below the minimum value for wetting of the solid surface. Accurate estimation of the critical shapes of the melt/solid and meniscus shapes for the movement of the meniscus across the a solidification surface requires knowledge of the wetting angles for the melt on its solid. A bound on the loss of the floating zone by this mechanism occurs when the meniscus and a melt/solid interface intersect. This limit is sometimes called the "Heywang limit" after the first researchers to observe the phenomena [26,27]. Coriell et al. [14] have shown that the Heywang or dewetting limit is operative in silicon floating zones bigger than 1 cm in diameter. The capillary instability that results from loss of the static shape was only observed in smaller silicon zones.

Microgravity floating zone experiments should overcome the stability limits caused by the effect of gravity on meniscus shape and make possible crystal growth with long molten zones [28]. Calculations [8,25] and experiments for a liquid zone bordered by non-interacting cylinders [28] would place the maximum zone length at the value $2\pi R_0$ predicted by the Rayleigh–Plateau instability [29,30] for a cylindrical zone; the adjustments in this value necessary to account for non-cylindrical liquid volumes have been reported [16]. These stability calculations neglect the important interactions of the length and volume of a steady-state zone with heat transfer. Calculations with the thermal-capillary model are used in section 4.4 to assess the differences between crystal growth on earth and in microgravity.

2. Conduction-dominated thermal-capillary model

The steady-state growth of silicon in a resistively heated floating zone is modelled using a conduction-dominated heat transfer model. When the heating is axisymmetric the computational domain for melt,

feed, and crystal rods can be taken as the meridional half-plane shown in fig. 1. Then the domain consists of the feed crystal (D_f) being input from above, the melt (D_m), and the growing crystal (D_c) that is being extracted from below. The boundaries of these domains (∂D_i) and their corresponding unit normal vectors (n_i, N_i) are also shown in fig. 1. We assume that the shapes of the melt/gas, melt/feed, and melt/crystal interfaces can be represented as single-values functions of one coordinate as shown there. These representations are used in the mathematical expression of the free-boundary problem and in the method used for its solution.

For a feed rod of constant radius (R_f) and translation rate V_f, steady-state growth is obtained with the crystal rod moving at speed V_c and growing with radius R_c, where $R_c^2 V_c = R_f^2 V_f$, assuming the densities of feed and crystal are the same. Dimensionless variables are defined using R_f as the length scale, the melting temperature of the material T_m as the temperature scale, and the speed V_f as the velocity scale. When steady-state is achieved, the lengths of the solid feed (L_1) and crystal (L_2) rods are usually many times their radii as measured from the origin of the cylindrical polar coordinate system with origin at the maximum of the ambient temperature distribution. Then a one-dimensional approximation to the temperature field should be accurate if heat loss from these phases to the ambient is controlled by conduction and radiation from the surface to the surroundings.

The scaling introduced below shows that one-dimensional approximations to the heat equations are indeed valid far from the melt/solid phase boundaries. The solution of the two-dimensional thermal-capillary model is required adjacent to these interfaces and in the melt. The one- and two-dimensional models are spliced together in the finite-element analysis in a manner analogous to the application of the method of matched asymptotic expansions [31] applied to similar problems in heat transfer where the solutions in each region can be computed in closed form [6,32]. The portions of the solids and the melt where the two-dimensional model is required constitute the "inner region". The lengths of crystal and feed rods included in this region are denoted as L_c and L_f, respectively; see fig. 1. The one-dimensional heat balances are incorporated into the finite-element analysis far away from the melt/solid interfaces – the outer regions – in order to simplify the numerical solution. This same strategy has been applied successfully before in the numerical solution of capillary statics [33] and viscous free-surface [34] problems.

2.1. Two-dimensional model: inner region

The conduction-dominated model for energy transport includes only conduction in the melt*,

$$\kappa \, \nabla^2 \theta = 0, \quad \text{in } D_m, \tag{1}$$

but includes convection due to the steady translation of the crystal and feed rods as

$$\nabla \cdot \left[k(\theta) \, \nabla \theta \right] - \text{Pe}_i(e_z \cdot \nabla \theta) = 0, \quad \text{in } D_i, \quad i = \text{c, f}, \tag{2}$$

where ∇ is the gradient operator in cylindrical coordinates, e_z is the unit vector in the axial direction, and κ is the ratio of thermal conductivities between melt and solid at the reference temperature T_{mp}, i.e. $\kappa \equiv k_{m,mp}/k_{s,mp}$. The function $k(\theta)$ is the dimensionless thermal conductivity in the feed and crystal phases which is typically a strong function of temperature. The conductivity in the melt is taken to be independent of temperature, since no experimental data relating its value to the temperature is available. The Peclet numbers based on the translation speeds are defined as $\text{Pe}_i \equiv V_i R_0/\alpha_s$ ($i = \text{c, f}$), where α_s is the thermal diffusivity of the solid evaluated at the reference temperature T_{mp}. As discussed below, the Peclet numbers based on the translation rate are low in both phases. We include the convective heat transport in

---

* Cf. Nomenclature at the end of this paper.

the solids only because the thermal conductivity of this phase is lower and because the kinematics of this phase is known. Inclusion of convection in the melt will require solution of the equations of motion and continuity because of the deformation of the meniscus and the melt/solid interfaces.

Heat transport between the two solid phases and the melt is dictated by the interfacial energy balances

$$\kappa[N_i \cdot \nabla\theta]_m - k(\theta)[N_i \cdot \nabla\theta]_i = -\text{Pe St}(N_i \cdot e_z), \quad \text{on } \partial D_{Ii}, \quad i = c, f, \tag{3}$$

where the brackets $[\cdot]_i$ signify a quantity evaluated at the interface in the indicated phase, and the Stefan number $\text{St} \equiv \Delta H / C_{ps} T_{mp}$ (see section 6) scales the heat released upon solidification to the sensible heat in the solid. The unit normal vectors to the crystal/melt and feed/melt interfaces are denoted as N_c and N_f, respectively. The latent heat of silicon is large enough to have an appreciable effect on the shapes of molten zones, as is shown by our calculations. Heat transfer from the floating zone to the ambient and heater is by both radiation and convection according to the energy balances along the melt

$$\kappa(n_m \cdot \nabla\theta) = \text{Ra}_m(\theta^4 - \theta_\infty^4) + \text{Bi}_m(\theta - \theta_\infty), \quad \text{on } \partial D_m, \tag{4a}$$

and along the boundaries of the solid rods

$$k(\theta)(n_i \cdot \nabla\theta) = \text{Ra}_i(\theta^4 - \theta_\infty^4) + \text{Bi}_i(\theta - \theta_\infty), \quad \text{on } \partial D_i, \quad i = c, f, \tag{4b}$$

where n_i, $i = m, c, f$, are the unit normal vectors along the surfaces of the melt, crystal and feed regions of the zone, respectively. The radiation ($\text{Ra}_i \equiv \sigma \epsilon R_i T_{mp}^3 / k_{s,mp}$) and Biot ($\text{Bi}_i \equiv h R_i / k_{s,mp}$) numbers are both $O(10^{-2})$ for the thermophysical properties characteristic of small-scale silicon floating zones; this point is exploited in section 2.2.

The centerline ($r = 0$) is an axis of symmetry in all three phases:

$$e_r \cdot \nabla\theta = 0, \quad \text{on } \partial D_0, \tag{5}$$

where e_r is the radial unit vector. The locations of the two melt/solid interfaces are specified by the condition for an equilibrium melting temperature of the material:

$$[\theta]_m = [\theta]_c = [\theta]_f = 1, \quad \text{on } \partial D_{Ic} \text{ and } \partial D_{If}. \tag{6}$$

The assumption of a specified melting temperature is valid for slow growth rates and materials with atomically rough solidification interfaces. The variation of melting temperature caused by the curvature of the melt/solid interface is neglected because this effect is extremely small for the curvatures characteristic of millimeter or larger floating zone systems.

The heat exchange between the heater, ambient and the zone is dictated by the ambient temperature distribution $\theta_\infty(z)$ specified along the zone length. We model the temperature distribution from a radiant heat source by the Gaussian distribution given in dimensionless form as

$$\theta_\infty = (\theta_m - \theta_\infty^0) \exp\left[-(z/\sigma)^2\right] + \theta_\infty^0, \tag{7}$$

where θ_m is the maximum temperature at the center of the heater, σ is the width of the distribution, and θ_∞^0 is the ambient temperature away from the heater. Other forms of the ambient profile can be incorporated easily into the finite element solution method; an example is given in section 5. We neglect the complications of computing the view factors from points along the surface of the zone to the ambient profile, eq. (7). Setting the view factors to unity with a specified ambient profile corresponds to having this distribution imposed on a surface in close proximity to the three phases of the zone. This is probably optimal for good thermal control of the system.

We assume that the shape of the melt/gas meniscus is governed by the Young–Laplace equation of capillary statics

$$2\lambda + Gz = 2H, \tag{8}$$

where H is the mean curvature of the meniscus defined as

$$2H = \frac{f_{zz}}{\left(1 + f_z^2\right)^{3/2}} - \frac{1}{f\left(1 + f_z^2\right)^{1/2}}, \tag{9}$$

$G \equiv gR^2\Delta\rho/\gamma$ is the gravitational Bond number measuring the relative effects of gravity and surface tension (γ) in setting meniscus shape, and $\lambda = \Delta p_0 R_f/\gamma$ is a dimensionless reference pressure difference necessary to set the volume of the molten zone. Implicit in eq. (8) is the fact that viscous stress along the meniscus has only a small effect on the shape; neglecting this force is justified by the low capillary number typical of semiconductor melts for melt velocities up to 100 cm/s [8].

The solution of the second-order, boundary-value problem (eqs. (1)–(6)) for the shape of the melt/gas meniscus requires three boundary conditions to set the locations of the ends of the interface and to determine λ. Obviously, the meniscus must join the melt/solid interfaces at the tri-junctions:

$$f(h_L(R)) = R, \quad f(h_U(1)) = 1, \tag{10}$$

where $R \equiv R_c/R_f$ is the radius ratio. The additional constraint for determining the reference pressure during steady solidification is taken from the the condition that the angle ϕ_0 between the tangents to the melt/gas and crystal/gas interfaces at a growing crystal interface is a material property [35,36]. For a steadily growing crystal this condition can be written as

$$[df/dz]_{z=h_L(1)} = \tan \phi_0. \tag{11}$$

The more complete formulation of this condition necessary for specifying the dynamical version of the thermal-capillary model will be presented in a later publication. The growth angle ϕ_0 is approximately 11° for silicon growing on the $\langle 111 \rangle$ surface [36].

2.2. One-dimensional model: outer region

For small Biot and radiation numbers, the temperature field varies significantly only in the axial direction, except in the solid regions near the melt/solid interfaces where thermophysical properties change abruptly and latent heat is released, and in the melt where the energy input from the heater can vary appreciably along the axis. Outside of these regions a one-dimensional energy balance is valid for approximating the temperature in the solid phases [32]. The one-dimensional model is formed by defining a radially-averaged temperature as

$$\bar{\theta}(z) \equiv 2\int_0^1 \theta(r, z)\, r \, dr, \tag{12a}$$

in the feed rod, and

$$\bar{\theta}(z) \equiv \frac{2}{R_c^2} \int_0^{R_c} \theta(r, z)\, r \, dr, \tag{12b}$$

in the growing crystal. The radially averaged energy balance in the solid phases is defined by

$$\frac{d}{dz}\left(k(\bar{\theta})\frac{d\bar{\theta}}{dz}\right) + \frac{Pe_i}{R_i}\frac{d\bar{\theta}}{dz} = \frac{Pe_i}{R_i^2}\left[Ra_i\left(\bar{\theta}^4 - \theta_\infty^4\right) + Bi_i\left(\bar{\theta} - \theta_\infty\right)\right], \quad i = c, f. \tag{13}$$

The solutions of eqs. (13) are spliced to the temperature field predicted by the two-dimensional model by relating the temperature fields using the definitions of the radially-average temperatures, eqs. (12), and by matching the temperature gradients at the specied boundaries ($z \equiv L_f = H_1$ and $z \equiv -L_c = H_2$) of the inner and outer regions. At the ends of the outer region ($z = L_1$ and $z = -L_2$), either the heat flux is set to zero or the temperature is specified. The first condition is used in all the calculations for proto-type floating zones described in section 4; the second condition is used in the comparison to experiments presented in section 5.

3. Finite element analysis

The nonlinear free-boundary problem defining the steady-state temperature field, the solidification interfaces, and the meniscus shape is solved using a generalization of the isotherm/Newton method developed by Ettouney and Brown [37]. The Galerkin finite element technique is used to discretize the entire problem and the resulting nonlinear set is solved by Newton's method. To implement Newton iterations for the unknown boundary shapes requires evaluating the sensitivity coefficients of the Galerkin residual equations with respect to changes in the boundary shapes at each iteration. This dependence is implicit in the free-boundary problem through the shape of the melt, feed, and crystal regions. We make the dependencies of the equations on the interface locations explicit by transforming the equation set to the fixed cylindrical region in the (ω, ζ) coordinate system shown in fig. 2. The necessary non-orthogonal mappings, and the original and reciprocal basis vectors are listed in table 2. The gradient operator ∇ appearing in the energy equations and boundary conditions is defined as

$$\nabla \equiv e^\omega(\partial/\partial\omega) + e^\zeta(\partial/\partial\zeta), \tag{14}$$

in terms of the reciprocal basis vectors. The shapes of the interfaces appear explicitly in ∇ through the definitions of (e^ω, e^ζ) given in table 2.
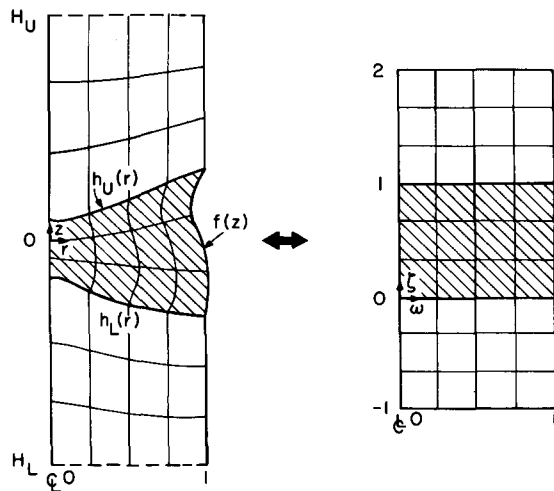

Fig. 2. Computational domain in transformed coordinates.

Table 1
Dimensionless groups and operating values used in the analysis of small-scale floating zone crystal growth for silicon

Parameter	Small-scale zone	Microzone
Radius of crystal and feed rods (cm)	1.0	0.275
Growth velocity (cm/min)	0.25	0.01
Growth angle ϕ_0 (deg)	11	11
Stefan number, St	1.07	1.07
Ambient temperature, θ_∞^0	0.2	0.2
Maximum heater temperature, θ_m	1.5	1.053
Width of heater temperature profile, σ	1.45	34.4
Emissivity ratio ϵ_m/ϵ_s	1.0	0.45
Thermal conductivity ratio at the reference temperature T_{mp}, $k_m(T_{mp})/k_s(T_{mp})$	2.9	2.9
Peclet number, Pe_c	0.05	0.0005
Radiation numbers, Ra_c, Ra_f	0.081	0.024
Biot numbers, Bi_c, Bi_f	0.005	0.0
Bond number, G	3.5	0.262

The cylindrical domain in (ω, ζ) coordinates is divided into quadrilateral elements. The temperature field in all three phases is approximated using the 9-node Lagrangian biquadratic basis functions $\{\Phi^i(\xi, \eta)\}$ defined on a unit element $(-1 \leqslant \xi \leqslant 1, -1 \leqslant \eta \leqslant 1)$ in the usual way as

$$\theta(\omega(\zeta, \eta), \zeta(\xi, \eta)) \equiv \sum_{i=1}^{9} \vartheta_i \, \Phi^i(\xi, \eta), \tag{15}$$

where $\{\vartheta_i\}$ are coefficients determined by solution of the Galerkin weighted residual equations. The coordinates in the transformed domain (ω, ζ) and those defining the unit element are connected using the isoparametric transformation

$$\omega \equiv \sum_{i=1}^{9} \omega_i \, \Phi^i(\xi, \eta), \quad \zeta \equiv \sum_{1=1}^{9} \zeta_i \, \Phi^i(\xi, \eta), \tag{16}$$

where the (ω_i, ζ_i) are the nodal coordinates of the finite element discretization. The interface shape functions $(f(\zeta), h_1(\omega), h_2(\omega))$ are approximated by finite element expansions in one-dimensional quadratic basis functions $\{\Gamma^i(\zeta)\}$ written in the transformed coordinates as

$$f(\zeta) \equiv \sum_{i=1}^{3} f_i \, \Gamma^i(\zeta), \quad h_1(\omega) \equiv \sum_{i=1}^{3} h_{1i} \, \Gamma^i(\omega), \quad h_2(\omega) \equiv \sum_{i=1}^{3} h_{2i} \, \Gamma^i(\omega), \tag{17}$$

for each one-dimensional element along a boundary.

The energy equations in each phase are discretized using the Galerkin finite element method in the same way as avocated in the isotherm/Newton technique introduced by Ettouney and Brown [37]. The natural conditions, eqs. (3) and (4), along phase and external boundaries are combined with the field equations to yield a set of algebraic equations expressed in terms of the unknown coefficients in the expansions, eqs.

(15) and (17). The energy balances become

$$\int_{D_m} \kappa \, \nabla\Phi^i \cdot \nabla\theta \, dV + \int_{\partial D_m} \Phi^i \left[\mathrm{Ra}_m \left(\theta^4 - \theta_\infty^4 \right) + \mathrm{Bi}_m \left(\theta - \theta_\infty \right) \right] dS + \int_{\partial D_{1c}} \mathrm{Pe}_c \, \mathrm{St} \, \Phi^i \left[N_c \cdot e_z \right] dS$$

$$+ \int_{\partial D_{1f}} \mathrm{Pe}_f \, \mathrm{St} \, \Phi^i \left[N_f \cdot e_z \right] dS = 0, \quad i = i, \ldots, N_m, \tag{18}$$

$$\int_{D_j} \left[k(\theta) \, \nabla\Phi^i \cdot \nabla\theta + \mathrm{Pe}_j \, \Phi^i \left(e_z \cdot \nabla\theta \right) \right] dV + \int_{\partial D_j} \Phi^i \left[\mathrm{Ra}_j \left(\theta^4 - \theta_\infty^4 \right) + \mathrm{Bi}_j \left(\theta - \theta_\infty \right) \right] dS$$

$$+ \int_{\partial D_{1j}} \mathrm{Pe}_j \, \mathrm{St} \, \Phi^i \left(N_j \cdot e_z \right) dS = 0, \quad i = 1, \ldots, N_j, \quad j = c, f, \tag{19}$$

where the $\{ N_j \}$, $j = m$, c, f, are the numbers of unknowns in the finite element expansion for the temperature field in each phase. The integrals in eqs. (18) and (19) are defined on the transformed regions in the (ω, ζ) coordinate system, as represented by notation for the original coordinate system shown on fig. 1. The locations of the melt/solid interfaces are determined by forming the residual equations for the isotherm conditions eq. (6) as

$$\int_{\partial D_{1j}} \Gamma^i \left(\theta - 1 \right) dS = 0, \quad i = 1, \ldots, M_j, \quad j = c, f, \tag{20}$$

where $\{ M_j \}$ are the number of unknowns in the finite element expansions for the melt/crystal ($j = c$) and melt/feed ($j = f$) interfaces, respectively, and the $\{ \Gamma^i(x, y) \}$ are the one-dimensional Lagrangian quadratic functions defined along these boundaries. The Galerkin equations for the residual equations in the inner region are spliced to approximations in the outer region at the mathematical boundaries shown in fig. 1. The temperature field in the outer regions are expressed in terms of one-dimensional quadratic approximations as

$$\bar{\theta}(\zeta) \equiv \sum_{i=1}^{3} \bar{\vartheta}_i \, \Gamma^i(\zeta). \tag{21}$$

The weighted residual equations for the energy equations in the outer region are written as follows: for the crystal,

$$\int_{-L_2}^{-L_c} \left[\frac{d\Gamma^i}{dz} \frac{d\bar{\theta}}{dz} k(\bar{\theta}) - \mathrm{Pe}_c \, \Gamma^i \frac{d\bar{\theta}}{dz} + 2 \left[\mathrm{Ra}_c \left(\bar{\theta}^4 - \theta_\infty^4 \right) + \mathrm{Bi}_c \left(\theta - \theta \right) \right] \right] dz + \left[\Gamma^i k(\bar{\theta}) \frac{d\bar{\theta}}{dz} \right]_{\zeta = -L_c} = 0; \tag{22a}$$

for the feed rod,

$$\int_{L_f}^{L_1} \left[\frac{d\Gamma^i}{dz} \frac{d\bar{\theta}}{dz} k(\bar{\theta}) - \mathrm{Pe}_f \, \Gamma^i \frac{d\bar{\theta}}{dz} 2 \left[\mathrm{Ra}_f \left(\bar{\theta}^4 - \theta_\infty^4 \right) + \mathrm{Bi}_f \left(\bar{\theta} - \theta_\infty \right) \right] \right] dz - \left[\Gamma^i k(\bar{\theta}) \frac{d\bar{\theta}}{dz} \right]_{z = L_f} = 0, \tag{22b}$$

where the index i is over all the basis functions in the one-dimensional expansions, eqs. (21). The heat fluxes at the ends of the crystal and feed rods have been set to zero. The last term in each equation represents the matching of the heat fluxes with the two-dimensional temperature field on the interior region at the boundaries ∂D_{mf} and ∂D_{mc}, by the definition of the radially-averaged temperature, eq. (12a).

Table 2
Transformations for melt, crystal, and feed-rod regions of the computational domain

Melt

Transformation:

$$\omega \equiv \frac{r}{f(\zeta)}, \quad \zeta \equiv \frac{z - h_L(\omega)}{h_U(\zeta) - h_L(\zeta)}, \quad \phi \equiv \phi$$

Base vectors:

$$e_\omega \equiv f(\zeta)e_r + [(h'_U - h'_L)\zeta + h'_L]e_z, \quad e_\zeta \equiv \omega f'(\zeta)e_r + (h_U - h_L)e_z, \quad e_\phi \equiv \omega f e_\phi$$

Reciprocal base vectors:

$$e^\omega \equiv [\omega f(h_U - h_L)e_r - \omega^2 ff'e_z]/B$$

$$e^\zeta \equiv [\omega f(h'_U - h'_L)\zeta + h'_L)e_r + \omega f^2 e_z]/B$$

$$e^\theta \equiv [f(h_U - h_L)\omega - \omega f\{(h'_U - h'_L)\zeta + h'_L\}]e_\theta/B$$

$$B \equiv \omega f^2(h_U - h_L) - \omega^2 ff'[(h'_U - h'_L)\zeta + h'_L]$$

Crystal (lower solid)

Transformation:

$$\omega \equiv r, \quad \zeta \equiv \frac{z - H_1}{h_L - H_1} - 1, \quad \phi \equiv \phi$$

Base vectors:

$$e_\omega \equiv e_r + (\zeta + 1)h'_L e_z, \quad e_\zeta \equiv (h_L - H_1)e_z, \quad e_\phi \equiv e_\phi$$

Reciprocal base vectors:

$$e^\omega \equiv e_r, \quad e^\zeta \equiv \frac{(1 - \zeta)}{(h_L - H_1)}h'_L e_r + \frac{1}{h_L - H_1}e_z, \quad e^\phi \equiv e_\phi$$

Crystal (upper solid)

Transformation:

$$\omega \equiv r, \quad \zeta \equiv \frac{z - h_U}{H_2 - h_U} + 1, \quad \phi \equiv \phi$$

Base vectors:

$$e_\omega \equiv e_r + (2 - \zeta)h'_U e_z, \quad e_\zeta \equiv (H_2 - h_U)e_z, \quad e_\phi \equiv e_\phi$$

Reciprocal base vectors:

$$e^\omega \equiv e_r, \quad e^\zeta \equiv \frac{-h'_U(2 - \zeta)}{(H_2 - h_U)}e_r + \frac{1}{(H_2 - h_U)}e_z, \quad e^\phi \equiv e_\phi$$

The Galerkin weighted residual of the Young–Laplace equation is

$$\int_{h_1(R)}^{h_2(1)} \left\{ \Gamma^i \left[(Gz + 2\lambda)f(1 + f_z^2)^{1/2} + 1 \right] + \left[\Gamma^i f_z + f\Gamma_z^i \right] \tan^{-1}f_z \right\} dz = 0, \quad i = 1, \ldots, M_m, \tag{23}$$

where M_m is the number of unknowns in the expansion for the meniscus shape. Eq. (23) is solved simultaneously with the constraint that the meniscus pins on the edges of the feed and crystal rods. The condition for the steady state growth angle at the tri-junction on the growing crystal [10] is used to determine the reference pressure difference λ across the melt.

The complete set of residual equations described by eqs. (18)–(20), (22) and (23) can be expressed as

$$R(x) \equiv R(\theta, \bar{\theta}, f, h_1, h_2, \lambda) = 0, \tag{24}$$

for the coefficients in the temperature field, the shapes of the three interfaces and the reference pressure difference in terms of parameters appearing in the thermal-capillary model. The dependences of each of the variables on each other are explicit in the entire equation set, because of the non-orthogonal transformations used to map the problem to a cylindrical domain. When expressed in this form the complicated free-boundary problem describing the floating zone looks much less formidable.

The nonlinear equation set is solved by Newton's method simultaneously for the field and interface variables. Starting from an initial approximation to the vector of unknowns x^0, successive updates are constructed as

$$x^{n+1} = x^n + \delta^n, \tag{25}$$

and the correction vector δ^n is the solution of the linear equation set

$$J(x^n) \, \delta^{n+1} = -R(x^n), \tag{26}$$

where the components of the Jacobian matrix J are formed by explicit differentiation as $J_{ij} \equiv \partial R_i / \partial x_j$. The Newton iterations converge quadratically to solutions of the free-boundary shapes and the temperature field, as described in other publications [37,38]. The accuracy of the finite element approximations used for the floating zone and the effect of splicing together the two- and one-dimensional descriptions of the temperature field are discussed in section 4.1.

4. Numerical results

The thermophysical properties used to model silicon crystal growth are listed in table 3 and are similar to the values used in the calculations in ref. [22]. The only major difference is in the emissivities of molten and crystalline silicon, which are reported to differ by a factor of two in ref. [39], compared to earlier measurements where they were reported to be almost equal. All values except the thermal conductivity of solid silicon were assumed to be independent of changes in temperature. The conductivity of the solid was assumed to vary according to

$$k(\theta) \equiv 1/\theta, \tag{27}$$

as given by Bell [42]. The resulting dimensionless groups for a silicon floating zone with $R_f = R_c = 1.0$ cm

Table 3
Thermophysical properties used to model silicon crystal growth

Property	Value	Reference
Thermal conductivity of the melt	0.64 W/K·cm	[39]
Thermal conductivity of the solid at $T = T_{mp}$	0.22 W/K·cm	[39]
Heat capacity of the solid	1.038 J/g·K	[39]
Heat capacity of the melt	1.059 J/g·K	[39]
Heat of fusion	1803 J/g	[39]
Melting temperature	1695 K	[39]
Emissivity of solid	0.7	[39,40]
Emissivity of melt	0.3	[40]
Density of melt	2.55 g/cm³	[39]
Density of solid	2.33 g/cm³	[39]
Three-phase contact angle	11°	[36]
Surface tension	720 dyn/cm²	[41]

Table 4

Effect of mesh size and matching lengths on finite element predictions of interface shape and temperature gradients; the elements in mesh I are equally spaced in both the axial and radial directions; the elements in meshes II and III are graded toward the melt/solid interfaces to better resolve the temperature field in these regions

	Mesh I	Mesh II		Mesh III	
Number of axial elements in each region	6	12		24	
Total number of unknowns	623	1103		1779	
cpu time per Newton iteration (min)	2.63	6.43		10.00	
Lengths of two-dimensional Regions	$6R_f$	$6R_f$	$12R_f$	$6R_f$	$12R_f$
$[\partial\theta/\partial z]z = h_L(0)^-$	0.1822	0.1579	0.1500	0.1556	0.1420
$[\partial\theta/\partial z]z = h_U(0)^+$	−0.1323	−0.0894	−0.0670	−0.0885	−0.0670
$h_L(0)$	−0.6360	−0.6070	−0.5359	−0.6044	−0.5352
$h_L(1)$	−0.7274	−0.7196	−0.6908	−0.7189	−0.6918
$h_U(0)$	0.2074	0.1749	0.0919	0.1720	0.0915
$h_U(1)$	0.4735	0.4631	0.4509	0.4626	0.4507

are given in table 1. Calculations were performed on a Data General MV8000-II minicomputer in the Department of Chemical Engineering at MIT.

4.1. Accuracy of finite element analysis

Results are listed in table 4 for the values of the dimensionless groups given in table 1 for the 1 cm radius feed and crystal rods and $Pe_f = Pe_c = 0.05$ with three different finite element meshes and two values for the matching distances for the inner and outer regions. The melt/feed-rod interface was extremely deformed for this set of parameters. The meshes each have 6 elements spanning the radial direction in each of the three phases, but differ in the numbers of elements in the axial direction in the inner and outer regions. The number of axial elements is the same for each of the phases and the outer regions and is given in table 4. The elements in the crudest mesh (I) were equally spaced along the axis of the zone. The axial elements in the finer meshes were graded to be smallest adjacent to the melt/solid interfaces.

For $H_1 = H_2 = 6$, the values for the locations of the melt/solid interfaces at the centerline and edge of the zone and the temperature gradients along the centerline at these interfaces are converging with mesh refinement. The sensitivity of the location of the interface to mesh refinement is indicative of the sensitivity of the temperature field, because of the use of the isotherm condition as the distinguished condition in eq. (19). The shape of the melt/crystal interface and the temperature gradient there are less sensitive to mesh refinement because this interface is flatter than the upper solidification surface. The effect of increasing the lengths of the inner regions is most clearly seen by comparing the results for meshes II and III with the lengths of 6 and 12, respectively, because the axial elements in these two calculations are of approximately the same size. The two sets of results are similar, except for the interface positions and temperature gradients at the centerline, where the assumption of a radially uniform temperature field is expected to be poorest. Calculations with the longer matching lengths ($L_c = L_f = 12$) are more accurate.

Because the discrepancies between the results of meshes I and III are confined to parameter ranges where the melt/feed-rod interface is extremely curved, we have used the crude mesh (I) for all the calculations reported in section 4. These results are approximate, but can be improved by systematic mesh refinement.

4.2. Varying pull rates

The importance of the growth rate in setting the operation of the floating zone lies in the release and
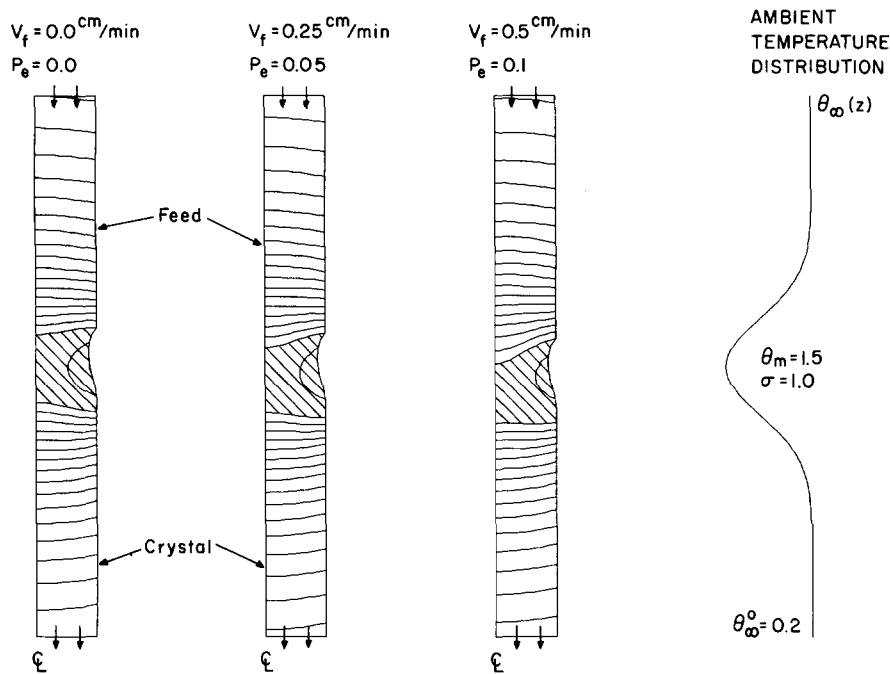
Fig. 3. Zone shapes and temperature fields for increasing pull rate (Peclet number), for $R_f = R_c = 1.0$ cm. Results correspond to (a) 0 cm/min, (b) 0.25 cm/min, and (c) 0.5 cm/min. Isotherms are spaced at $\Delta\theta = 0.025$.

extraction of latent heat at the melt/solid interfaces, not in the heat transport by convection of the solids. Fig. 3 shows zone shapes and isotherms for crystal growth rates ranging from 0 to 0.5 cm/min for a zone with feed and crystal rods of 1 cm radius. The molten zone translates toward the crystal and the curvature of the melt/crystal and melt/feed interfaces increases as the growth rate is increased. For the highest growth rate the zone is almost entirely downstream of the maximum in the heater profile and the temperature field in the melt is far from symmetric about the center of the zone. The solidifying interface becomes more concave to the melt and the melting interface becomes more convex to accommodate the release and uptake of latent heat, respectively, as the growth rate is increased.

Another, not so obvious, effect of increased growth rate is its effect on the position of the molten zone relative to the heat source. Increasing the translation rate moves the melt downward (see fig. 3) leaving the neck of the meniscus exposed to the hottest part of the heater. This reduction in surface area of the meniscus reduces heat transport to the zone, as demonstrated in section 4.3.

4.3. Meniscus shape: variation of bond number and growth angle

The coupling between the shape of the molten zone and the heat transfer in all three phases is set primarily by the effects of meniscus curvature on the surface area available for absorbing the radiant heat from the source. The results of calculations with increasing Bond number G for a zone with $R_c = R_f = 1$ cm and a pull rate of 0.25 cm/min are shown as fig. 4. For $G = 0$, the zone shape is nearly symmetrical about the center of the heater profile and the volume of the zone is larger than that of a cylinder with the same radius. Increasing the Bond number G causes the upper portion of the melt to sag, lowering the effective surface area for heat exchange with the ambient. The maximum temperature in the zone decreases and the length of the molten zone shrinks with increasing G, as shown by figs. 4b and 4c. The temperature
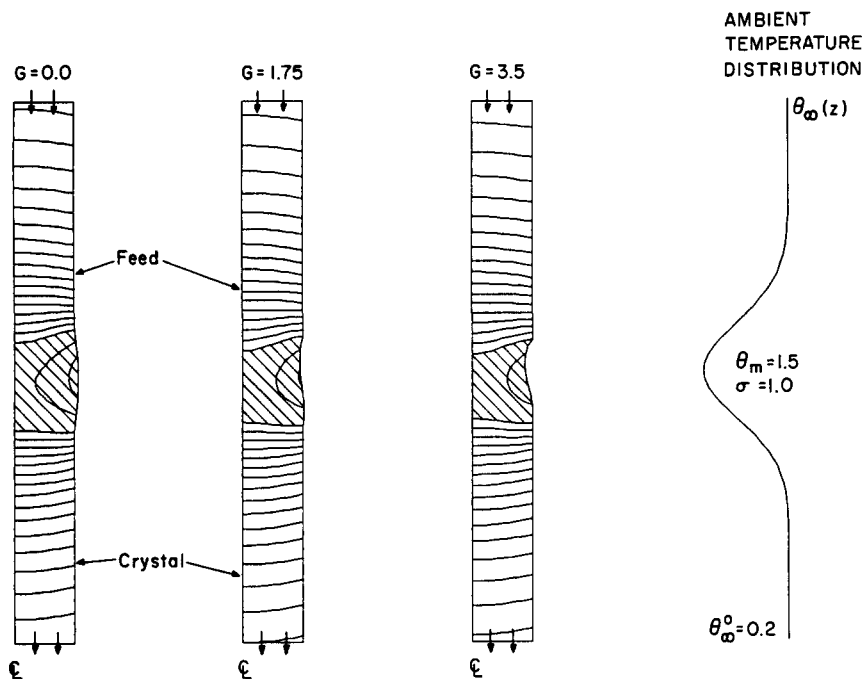
AMBIENT
TEMPERATURE
DISTRIBUTION

G = 0.0   G = 1.75   G = 3.5

$\theta_\infty(z)$

Feed

$\theta_m = 1.5$
$\sigma = 1.0$

Crystal

$\theta_\infty^0 = 0.2$

¢   ¢   ¢

Fig. 4. Zone shapes and temperature fields for increasing gravitational Bond number, for $R_f = R_c = 1.0$ cm and $\Delta\theta = 0.025$.

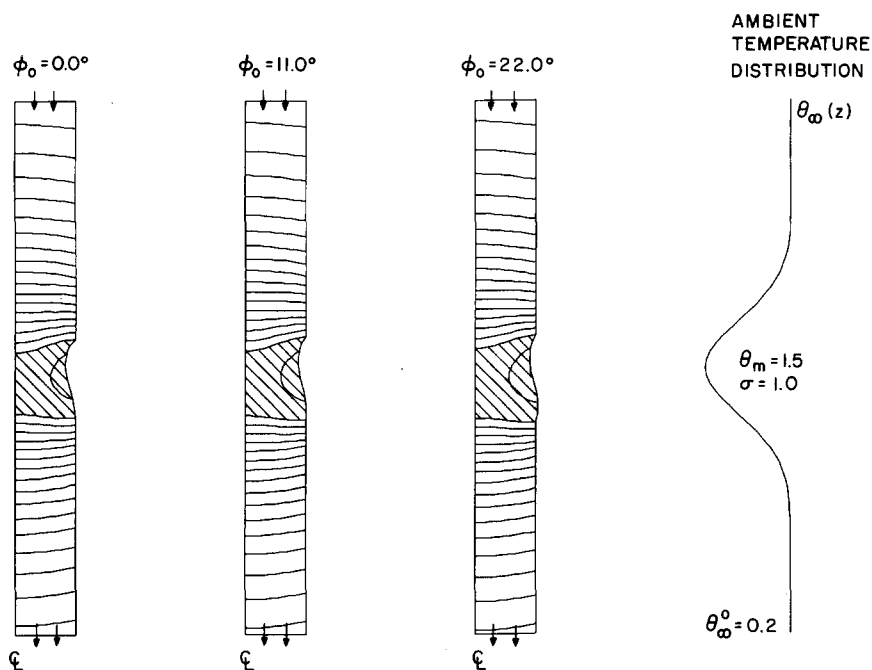AMBIENT
TEMPERATURE
DISTRIBUTION

$\phi_0 = 0.0°$ $\phi_0 = 11.0°$ $\phi_0 = 22.0°$

$\theta_\infty(z)$

$\theta_m = 1.5$
$\sigma = 1.0$

$\theta_\infty^0 = 0.2$

¢   ¢   ¢

Fig. 5. Zone shapes and temperature fields for increasing growth angle ϕ_0, for $R_f = R_c = 1.0$ cm and $\Delta\theta = 0.025$.

profile in the zone is not symmetric, but is distorted toward the growing crystal where the circumference of the meniscus is larger.

Increasing G while holding the shape of the heating profile constant leads to zone failure when the angle between the melt/gas and melt/feed-rod interfaces becomes less than the wetting angle for silicon melt on its solid. On earth, silicon zones with diameter larger than 1 cm fail by this mechanism, not by the capillary mechanism for loss-of-existence studied in refs. [13–16]. The decrease in the meniscus area exposed to the heater caused by increasing either G or Pe mitigates the thinning of the melt and the decreasing of the wetting angle at the feed rod. The wetting angle at the melting feed rod decreased only slightly with increasing G from 1.75 to 3.5. However, the shortening of the zone with increasing G also leads to the collapse of the melt by the joining of the feed and crystal rods. The zones shown in fig. 4 are destroyed by the intersection of the meniscus with the melt/feed-rod interface at $G = 7$.

The coupling between meniscus shape and heat transfer is also a function of the growth angle ϕ_0. The small uncertainty in ϕ_0, i.e. $\phi_0 = 11 \pm 1°$ in the experiments of Surek and Chalmers [36] had only small effects on the predictions of interface shapes and temperature fields. The changes in the zone shapes with large variations of ϕ_0 were more profound, as shown in fig. 5. A positive angle ($\phi_0 > 0°$) helps accommodate the weight of the melt without large deformations of the zone. Larger deformations occur for smaller angles (see fig. 5a). Loss of stability of the zone by the "de-wetting" of the feed rod is more likely for ϕ_0 close to zero when gravity is present.

Decreasing the emissivity of the melt reduced heat transport into the melt and shortened the zone length. We computed solutions of the thermal-capillary model using the lower melt emissivity of $\epsilon_m = 0.30$ suggested in ref. [40], which is consistent with the metallic surface of the melt. Results for the emissivity ratios of $\epsilon = 0.80$ and $\epsilon = 0.45$ are compared in fig. 6. No zone was possible for the lower value of
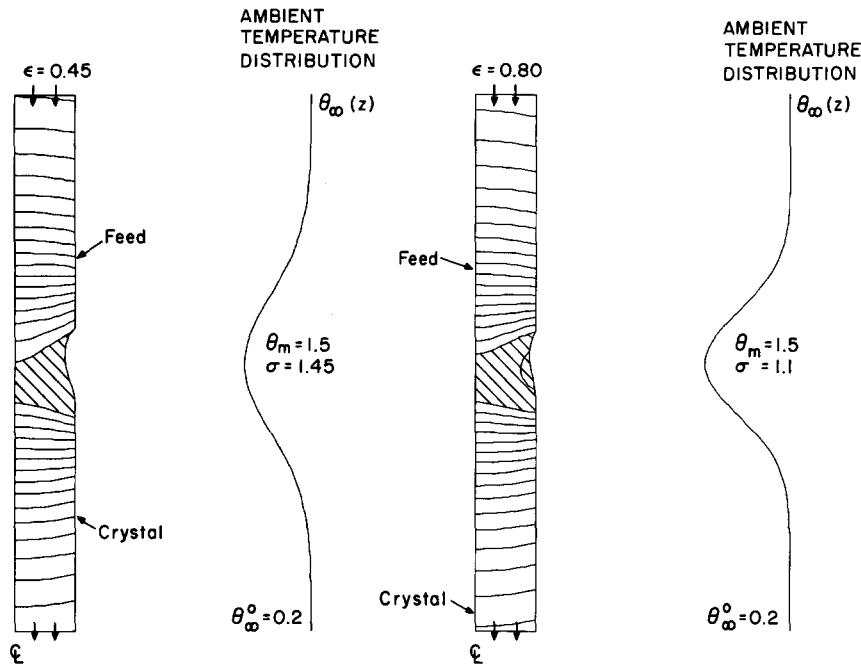

Fig. 6. Effect of change in melt emissivity ϵ_m on zone shape and temperature field. Calculations were performed with different ambient temperature distributions because calculations of steady-state solutions were impossible using the same temperature distribution. Isotherm spacing is $\Delta\theta = 0.025$.

emissivity and the ambient temperature profile using $\theta_m = 1.5$ and $\sigma = 1.1$. The heat input to the zone had to be increased by broadening the ambient profile by setting $\sigma = 1.45$. Heat flow into the feed rod from the ambient occurred for the broader ambient profile. The deflection of the melt/feed-rod interface was increased greatly; the possibility of dewetting the feed rod was enhanced with lengthening of the zone. Latent heat release from the melt/crystal interface forced heat to flow out of the crystal, even for the broaden ambient profile. Also, the melt was significantly cooler for the lower emissivity, as shown by the extra isotherm in the melt for the higher value of ϵ_m. No zone shape was possible with this larger heater and the larger emissivity ratio.

4.4. Varying zone size

Increasing the radii of the feed and crystal rods accentuates the effects of gravity on the shape of the melt and increases the two-dimensional nature of the temperature. Calculations were performed for earthbound zones with radii varying between 0.6 and 1.0 cm by systematically varying all the dimensionless parameters which are scaled with R_f; the pull rate was 0.25 cm/min. The overwhelming importance of zone shape on this set of calculations is noted from the quadratic dependence of G on the radius compared to the linear dependence in the other parameters (Pe_j, Bi_j, Ra_j). The heater profile was varied to keep its shape similar for all zone radii and the maximum heater temperature was fixed at $\theta_m = 1.5$. The zone shapes and thermal fields for these calculations are shown in fig. 7.

The two melt/solid interfaces eventually join as the diameter of the zone is increased, because of the decrease in the surface-to-volume ratio of the three phases. This tendency is evident in the results for $R_f = 1.0$ cm in fig. 7. Separated melt/solid interfaces were not found for $R_f > 1.1$ cm. The convex deflection (toward the melt) of the melt/feed-rod interface is responsible for the bridging of the two
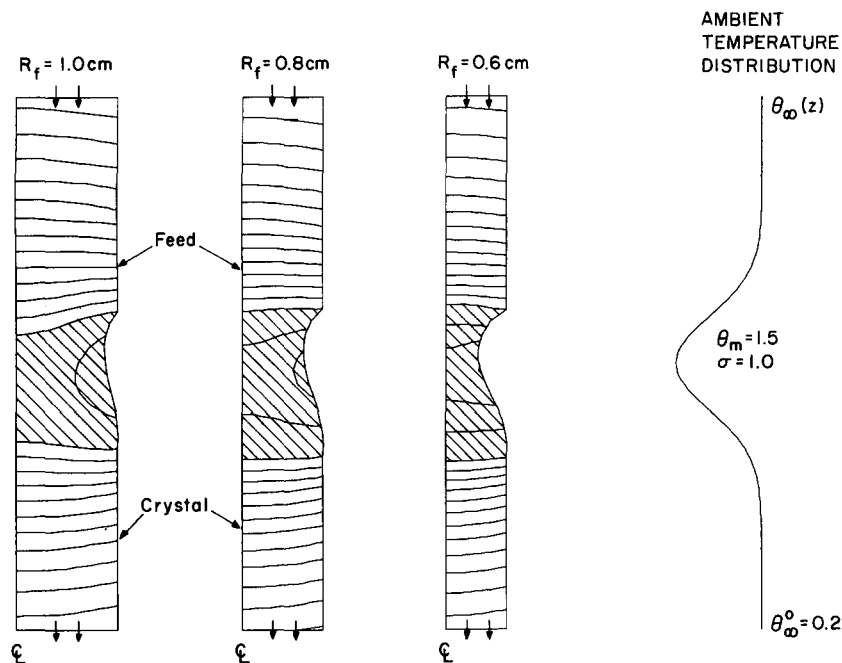

Fig. 7. Zone shapes and temperature fields for decreasing feed and crystal radii with the shape of the ambient temperature field held constant with respect to feed rod radius; isotherm spacing is $\Delta\theta = 0.025$.
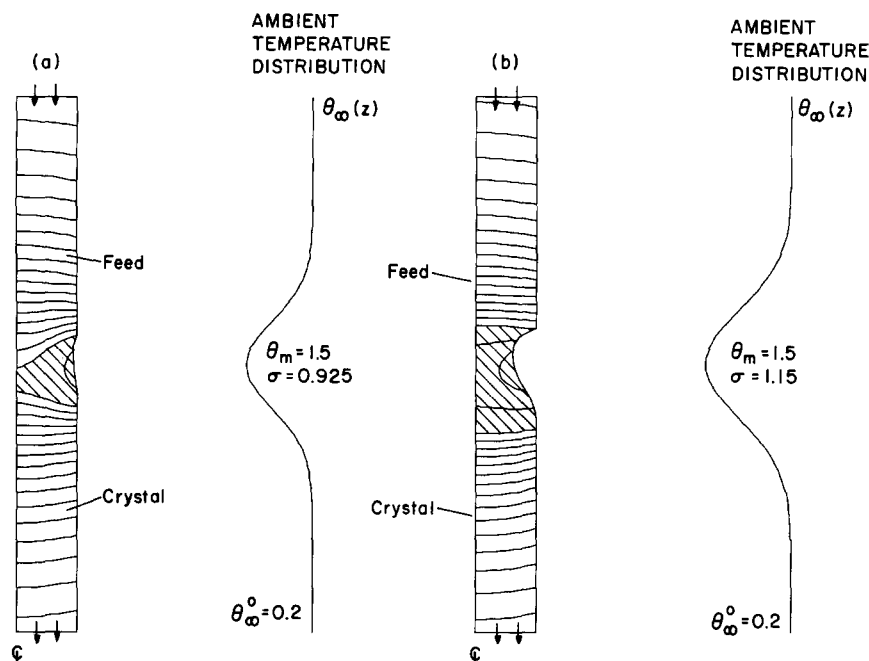
Fig. 8. Two extremes of zone shape achieved by varying the width of the ambient temperature profile. The cases correspond to failure of the zone by (a) bringing between the two melt/solid interfaces and (b) dewetting of the feed rod. Isotherm spacing is $\Delta\theta = 0.025$.

solidification fronts. Decreasing the translation rate lessens this effect by decreasing the requirement for latent heat and the convex deflection at this interface.

The results shown in fig. 7 are counter-intuitive in that the small diameter zones are more deformed than the zones with large diameter. This result is an artifact of forcing the size of the ambient temperature distribution to remain proportional to the radius of the feed and crystal rods; however, the sensitivity of the deformation accents the importance of the ambient temperature profile in setting the meniscus deformation, in conjunction with the Bond number and other parameters. Arguments that small zones will be less deformed or that a zone of a specific diameter will be less deformed at lower G are valid only if the aspect ratio of the molten zone is kept constant. Since the zone shape depends on heat transfer, it can only be surmised by solution of a thermal-capillary model.

4.5. Varying heater shapes

The mode of failure of the zone can be changed from the bridging of the two melt/solid interfaces to the dewetting of the feed rod by simply changing the width of the ambient temperature profile, as shown by the zone shapes in fig. 8, which were computed with all other parameters held constant at those listed in table 1. A small decrease in the width of the ambient profile from the value $\sigma = 0.925$ used in the computation in fig. 8a caused the interfaces to join; an increase to $\sigma = 1.15$ (see fig. 8b) caused the de-wetting of the feed rod.

Decreasing the maximum temperature θ_m has the same effect as decreasing σ; however, the zone shape is substantially more sensitive to θ_m because of the fourth-power dependence of the heat flux on the ambient temperature.

4.6. Pedestrial growth

Sample calculations of pedestal growth of large diameter crystals from small diameter feed rods are
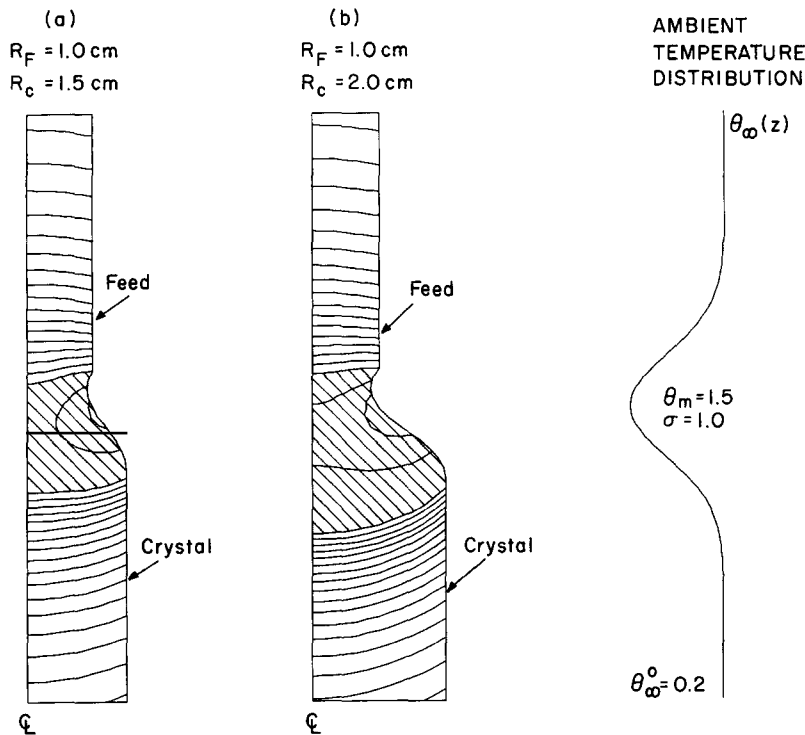
Fig. 9. Zone shapes and temperature fields for downward pedestal growth of large crystals from small feed rods. Calculations are for (a) $R_c/R_f = 1.5$ and (b) $R_c/R_f = 2.0$ with $R_c = 1.0$ cm and $\Delta\theta = 0.025$. The growth velocities of the feed rod are 0.111 cm/min and 0.0825 cm/min, respectively.

shown in fig. 9 for $R_f = 1.0$ cm and $R_c = 1.5$ and 2.0 cm. The translation rate of the feed rod was 0.25 cm/min in both cases and the pull rate of the crystal V_c was adjusted to maintain a steady-state zone size. Larger meniscus deformations are needed to hold together the melt volume for the growth of the larger crystal. The increase in the crystal size decreases the effectiveness of radial transport to the ambient, thereby resulting in steeper axial temperature gradients near the melt/crystal interface. The curvature of this solidification interface is also increased because of the larger radial temperature gradients in the lower crystal. The interface is concave toward the melt because of the release of latent heat. Increasing the size of the crystal radius changed the curvature of the melt/crystal interface from convex for the same heat transfer conditions to the concave shapes shown in fig. 9.

5. Comparison with experiments

Comparison of the predictions of the thermal-capillary model presented here with steady-state experiments requires careful characterization of the ambient temperature profile seen by the floating zone system. The shapes of the microzones given by Kim et al. [43] are similar to those predicted here, but cannot be matched with calculations because the ambient profile is not precisely specified. We have attempted such a comparison for the experiments of Kern [44] on a radiantly-heated small-scale zone. Unfortunately, the temperature field in these experiments was recorded only in a section of the furnace corresponding to a quarter of the length of the heater and the pull rate for the experiment was not
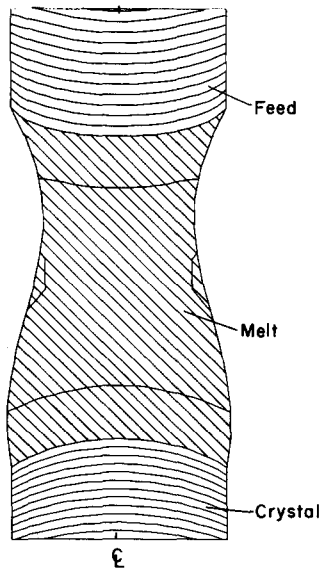
Fig. 10. Zone shape and temperature field for silicon microzone computed for ambient temperature distribution modelled after Kern's experiment. Isotherm spacing is $\Delta\theta = 0.001$.

reported. By correspondence with Kern it was ascertained that the cavity for the zone was 35 cm long with a 10 cm long heater in the center, and that the ends of crystal and feed rods were cooled to room temperature at the ends of the system. Calculations were performed using the dimensionless groups listed in table 1 with the emissivities ($\epsilon_m = 0.3$, $\epsilon_s = 0.7$) suggested in ref. [39]. The part of the ambient temperature profile measured by Kern was used to fit θ_m and σ in eq. (7).

We could not compute steady-state floating zones using the Gaussian ambient profile eq. (7) because this profile predicted too high an ambient temperature outside of the 10 cm region measured by Kern. We generalized eq. (7) to the three-parameter model

$$\theta_\infty(z) = (\theta_m - \theta_\infty^0)\frac{\exp\left[-(z/\sigma)^2\right]}{1 + CZ^{2n}} + \theta_\infty^0, \tag{28}$$

where σ and C were fit to the data of Kern for a given value of n. We were unsuccessful at finding steady-state solutions for $n < 4$. The parameter values ($n = 4$, $\theta_m = 1.053$, $\sigma = 34.4$) were used in the successful calculations.

The zone shape computed for a growth rate of 0.1 mm/min is shown in fig. 10. The length of the molten zone in the calculation was $3.4R_f$, which is in reasonable agreement with the value $3.5R_f$ measured by Kern from the rapidly quenched sample. The maximum temperature in the melt was 3.5 K above the melting point of silicon; Kern estimates this superheating to be 10 K in his experiments. Our calculations gave concave melt/crystal interfaces, which are not in agreement with the concave shapes reported by Kern. There are several possible explanations for this difference.

First, a very curved melt/crystal interface can only result from our model if the growth velocity, and hence the latent heat release, is increased substantially. We found that the molten zone was displaced substantially form the center of the heater at the growth rates necessary to model the interface shape seen by Kern. Secondly, the deflection of the melt/solid interfaces is very sensitive to the differences in the emissivity and thermal conductivity between the three phases. The parameters appropriate for Kern's

experiment may differ from our values. Also, for the slowly varying heater profile used by Kern, the solids near the molten zone absorb more heat than the adjacent melt, causing the solidification fronts to deflect towards the surfaces of the feed and crystal rods. The differences between our results and the experiment of Kern also may be due to either changes in emissivity with temperature or to the influence of view factors for radiation on the heat flux into the solids near the solidification interfaces.

6. Discussion

Coupling together heat transfer and capillarity in a model of the floating zone process leads to a quantitative interpretation of many physical phenomena observed in small scale zones. The interactions of zone length with the meniscus shape and gravity sheds new insight into the usefulness of low gravity processing and to changes in heater design and control that may be necessary for microgravity experiments. Increasing zone length, by varying either the heater profile or the level of gravity, increases the amount of meniscus sag, thereby decreasing the area of the meniscus near the heater. Heat transport into the zone is less effective the more deformed the interface. This effect is dampened for materials where the emissivitity of the melt is much lower than the solid, so that phase change leads to lower heat transfer.

The coupling between heat transport and meniscus shape partially explains why upward growth of a crystal by the floating zone technique is difficult to accomplish, except for very small crystals. Besides the difficulty with the top of the meniscus having a positive growth angle ϕ_0, upward translation of the zone results in the largest circumference of the meniscus being adjacent to the maximum temperature of the heater. Then small increases in growth rate can lead to large increases in heat transfer efficiency and to much longer zones, which in turn fail.

The calculations shown here demonstrate the approximate nature of many of the simplifying assumptions usually made when discussing the fluid mechanics of small scale floating zones. First, the melt volume is rarely cylindrical, except when the angel ϕ_0 is exactly zero and gravity is absent. The actual volume of melt present during steady-state growth depends on the coupling between heat transfer and capillarity and can only be found by the solution of a model like the one used here. Secondly, the temperature field in the melt is not symmetric with respect to the center plane of the external temperature distribution. Zone translation and the sag of the meniscus due to gravity distort the thermal field. Complete calculations of the thermal field, melt flow, and interface shapes are feasible by expanding the present finite element algorithm, as has been done for models of directional solidification [45]. These calculations are the best method for incorporating the complications in the flow caused by deformation of the molten zone.

We can estimate the magnitude of thermal-capillary and buoyancy-driven flows in a small-scale floating zone melt by using the temperature field in the calculations for Kern's system. To do this we use the velocity scales valid for rectilinear flows driven by either mechanism: surface-tension flow

$$V_\gamma^* \equiv (\partial\gamma/\partial T)[\Delta T]_a/\mu = O(10) \text{ cm/s}; \tag{28}$$

buoyancy-driven flow,

$$V_\beta^* = \rho\beta g R^2 [\Delta T]_r/\mu = O(1) \text{ cm/s}. \tag{29}$$

The parameters are defined in section 6 and $[\Delta T]_a$ and $[\Delta T]_r$ are estimates for the axial and radial temperature differences in the zone. The order-of-magnitude estimates are based on $[\Delta T]_a = 3.5$ K. Both predictions are likely to over-estimate substantially the magnitudes of the actual motions because of the retarding effects caused by the almost equal height and diameter of the melt and because the driving forces for both types of flow are nonuniform throughout the zone.

Accounting for the influences of heat transfer on capillarity leads to new interpretations of the roles of classical limits of stability derived for isothermal zones with the length of the melt being parametrically decoupled from the capillary problem for the shape of the meniscus. The disparities between the theoretical prediction from the dewetting limit for the maximum length of a silicon melt with observations for RF-heated floating zones has been used by Keller and Mühlbauer [3] to estimate the importance of magnetostatic levitation. They argue that it is this levitation force that leads to stable float zoning of large diameter silicon.

It seems likely that the meniscus in an RF-heated zone recedes across the very convex interface of the feed rod until it reaches a new stable equilibrium condition corresponding to a melt with smaller radius and height. The tri-junction between melt, crystal, and gas may not be sharp, as modeled here, but may consist of a thin molten film that covers the upper surface of the melting feed rod and that evolves continuously into bulk melt in the narrowest section of the zone. Then the needle-shaped coil geometry used in RF-heated systems may be thought of as a clever method for introducing heat locally into this melt and establishing a very concave melt/feed interface. Changes are necessary in our thermal-capillary model to analyze this type of system.

Even the analysis of the Rayleigh limit for the maximum length of a zone in zero gravity is complicated by the interactions of the zone shape and the temperature field. Calculations aimed at finding the Rayleigh limit for a cylindrical zone formed for $\phi_0 = G = 0$ did not show the subcritical bifurcation expected for isothermal systems [16] where the zone length cannot interact with its shape. The decrease in surface area of the melt caused by the deformations that lead to the Rayleigh–Plateau instability lead to a decrease in the heat transport to the zone and in the zone length. Overstable oscillations leading to a limit cycle are possible and will be investigated in another paper [46].

Although not complete, the match between the predictions of the thermal-capillary model used here and the experiments of Kern gives confidence that temperature fields, interface shapes and stability predictions made with such a model are valuable information in the understanding of real systems. Only the comparison between calculations and experiments given in [47] for silicon sheet growth by the EFG technique gives a more extensive test of a thermal-capillary model.

Nomenclature

Bi_i	Biot number in phase i, $hR_i/k_{s,mp}$
C_{pi}	Heat capacity in phase i [J/g · K]
D_i	Domain of phase i
∂D_i	Boundaries of phases; see fig. 1
e_r	ith unit vector in radial direction
e_z	Unit vector in axial direction
e_i	ith unit vector in transformed domain
e^i	ith reciprocal unit vector in transformed domain
f	Meniscus shape function
g	Gravitational acceleration [cm/s^2]
G	Bond number, $gR^2\Delta\rho/\gamma$
h	Heat transfer coefficient [W/cm^2 · K]
h_i	Position of ith melt/solid interface; see fig. 1
H_i	Positions of the boundaries between the inner and outer regions measured with respect to the origin at the center of the heater, $i = 1, 2$
J	Jacobian matrix
$J_{i,j}$	Components of Jacobian matrix

k_i Thermal conductivity of ith phase [W/cm · K]

L_i Lengths of the two-dimensional regions, $i = $ c, f

$\boldsymbol{n}_i$ Unit normal to surface i

$\boldsymbol{N}_i$ Unit normal to melt/solid interfaces; see fig. 1

N Number of unknowns in expansion for temperature in inner region

N_f Number of meniscus slope unknowns

$N_{h,i}$ Number of melt/solid interface unknowns, 1 = lower, 2 = upper

Pe_i Peclet number for ith phase, $V_i R_i \rho_s C_{p_s}/k_{s,mp}$

r Dimensionless radial coordinate measured from zone centerline

R Ratio of radii of crystal to feed rod, R_c/R_f

R_i Radius of crystal ($i = $ c) and feed ($i = $ f) rods

$\boldsymbol{R}$ Residual vector

R_i Component of residual vector

Ra_i Radiation number, $\sigma \epsilon R_i T_{mp}^3/k_{s,mp}$

St Stefan number, $\Delta H/C_{p_s} T_{mp}$

T Temperature [K]

T_{max} Maximum temperature of the heater distribution

T_m Melting point temperature [1685 K]

V_g Growth velocity [cm/min]

x Vector of solution unknowns

x_i Component of solution unknowns

z Dimensionless axial coordinate measured from center plane of heater

α Temperature unknown vector

α_i Component of α

γ Surface tension

Γ^i One-dimensional polynomial basis functions for interface shapes

δ Correction vector used in Newton's method

ΔH Heat of fusion [J/g]

Δp_0 Reference pressure at centertime and center plane of heater [dyn/cm^2]

$\Delta \rho$ Density difference across meniscus [g/cm^2]

ϵ_i Emissivity of melt ($i = $ m) and solid ($i = $ s) surfaces

ϵ Ratio of emissivities, ϵ_m/ϵ_s

ζ Transformed axial coordinate

η Axial coordinate in unit element

θ Dimensionless temperature, T/T_{mp}

ϑ_i Coefficients in finite element expansion for temperature

κ Ratio of thermal conductivities evaluated at the reference temperature, $k_{m,mp}/k_{s,mp}$

λ Dimensionless reference pressure, $\Delta p_0 R/\gamma$

ξ Radial coordinate for unit element

ρ_i Density $i = $ l, s

σ^* Stefan–Boltzmann constant [W/cm^2 · K^4]

σ Width of internal temperature distribution

ϕ Angular coordinate in both original and transformed coordinate systems

ϕ_0 Steady state growth angle

Φ^i Two-dimensional polynomial basis functions for temperature field

ω Transformed radial coordinate

Acknolwedgements

References

[1] W.G. Pfann, Met. Rev. 2 (1957) 29.
[2] W.G. Pfann, Zone Melting, 2nd ed. (Wiley, New York, 1966).
[3] W. Keller and A. Mühlbauer, Floating Zone Silicon (Dekker, New York, 1981).
[4] J.H. Braun and R.A. Pellin, J. Electrochem. Soc. 108 (1961) 969.
[5] N. Kobayashi, J. Crystal Growth 43 (1978) 417.
[6] H.K. Kuiken and P.J. Robinson, J. Crystal Growth 47 (1979) 29.
[7] C.E. Chang and W.R. Wilcox, Intern. J. Heat Mass Transfer 19 (1976) 355.
[8] G.M. Harriott and R.A. Brown, J. Fluid Mech. 126 (1983) 269.
[9] G.M. Harriott and R.A. Brown, J. Fluid Mech. 144 (1984) 403.
[10] N. Kobayashi, J. Crystal Growth 66 (1984) 63.
[11] C.-H. Chun and W. Wuest, Acta Astronautica 5 (1978) 681.
[12] G.M. Harriott and R.A. Brown, J. Crystal Growth 69 (1984) 589.
[13] S.R. Coriell, S.C. Hardy and M.R. Cordes, J. Colloid Interface Sci. 60 (1977) 126.
[14] S.R. Coriell, S.C. Hardy and M.R. Cordes, J. Crystal Growth 42 (1977) 466.
[15] R.A. Brown and L.E. Scriven, Phil. Trans. Roy. Soc. London A297 (1980) 51.
[16] L.H. Ungar and R.A. Brown, Phil. Trans. Roy. Soc. London A306 (1982) 347.
[17] T. Surek and S.R. Coriell, J. Crystal Growth 37 (1977) 253.
[18] B.-I. Fu and S. Ostrach, Numerical Solution of Floating Zone Crystal Growth, Department of Mechanical and Aeronautical Engineering, CWRU, January 1983.
[19] F. Preisser, D. Schwabe and A. Scharmann, J. Fluid Mech. 126 (1983) 545.
[20] H. Kimura, M.F. Harvey, D.J. O'Connor, G.D. Robertson and G.C. Valley, J. Crystal Growth 62 (1983) 523.
[21] H.M. Ettouney, R.A. Brown and J.P. Kalejs, J. Crystal Growth 62 (1983) 230.
[22] J.J. Derby and R.A. Brown, J. Crystal Growth 74 (1986) 605; 75 (1986) 227.
[23] C.J. Chang and R.A. Brown, J. Computat. Phys. 53 (1984) 1.
[24] J.J. Derby and R.A. Brown, Chem. Eng. Sci. 41 (1986) 37.
[25] L.H. Ungar and R.A. Brown, J. Computat. Phys., submitted.
[26] W. Heywang and G. Ziegler, Z. Naturforsch. 9a (1954) 561.
[27] W. Heywang, Z. Naturforsch. 11a (1956) 238.
[28] J.R. Carruthers and M. Grasso, J. Appl. Phys. 43 (1972) 436.
[29] J.A.F. Plateau, Statique Expérimentale et Théorique des Liquides Soumis aux Seules Forces Moléculaires (Gauthier-Villars, Paris, 1873).
[30] J.W.S. Rayleigh, Proc. Roy. Soc. (London) 29 (1879) 71.
[31] C.M. Bender and S.A. Orszag, Advanced Mathematical Methods for Scientists and Engineers (McGraw-Hill, New York, 1978).
[32] H.K. Kuiken, J. Eng. Math. 13 (1979) 97.
[33] F.M. Orr, Jr., R.A. Brown and L.E. Scriven, J. Colloid Interface Sci. 60 (1977) 137.
[34] K. Ruschak, J. Fluid Mech. 119 (1982) 107.
[35] C. Herring, in: The Physics of Powder Metallurgy Symposium (McGraw-Hill, New York, 1951).
[36] T. Surek and B. Chalmers, J. Crystal Growth 29 (1975) 1.
[37] H.M. Ettouney and R.A. Brown J. Computat. Phys. 49 (1983) 118.
[38] J.J. Derby, R.A. Brown, F.T. Geyling, A.S. Jordan and G.A. Nikolakopoulou, J. Electrochem. Soc. 132 (1985) 470.
[39] Y.L. Toulakian, R.W. Powell, C.E. Ho and P.G. Klemen, Thermophysical Properties of Matter (Plenum, New York, 1979).
[40] K.A. Jackson and D.A. Kurze, J. Crystal Growth 71 (1985) 385.
[41] S.V. Lukin, V.I. Zhuchkov, N.A. Vatolin and Y.U. Kozlov, J. Less-Common Metals 67 (1979) 407.
[42] A.E. Bell, RCA Rev. 38 (1977) 109.
[43] K.M. Kim, A.B. Dreeben and A. Schujko, J. Appl. Phys. 50 (1979) 4472.
[44] E.L. Kern, Microgravity Si Zoning Investigation, NASA Report, NAS8-34920, July 15, 1984.
[45] P.M. Adornato and R.A. Brown, Intern. J. Numer. Methods Fluids, submitted.
[46] J.L. Duranceau and R.A. Brown, J. Crystal Growth, in preparation.
[47] H.M. Ettouney, J.P. Kalejs and R.A. Brown, J. Crystal Growth 70 (1984) 306.